

# PCCP

Accepted Manuscript



This is an *Accepted Manuscript*, which has been through the Royal Society of Chemistry peer review process and has been accepted for publication.

*Accepted Manuscripts* are published online shortly after acceptance, before technical editing, formatting and proof reading. Using this free service, authors can make their results available to the community, in citable form, before we publish the edited article. We will replace this *Accepted Manuscript* with the edited and formatted *Advance Article* as soon as it is available.

You can find more information about *Accepted Manuscripts* in the [Information for Authors](#).

Please note that technical editing may introduce minor changes to the text and/or graphics, which may alter content. The journal's standard [Terms & Conditions](#) and the [Ethical guidelines](#) still apply. In no event shall the Royal Society of Chemistry be held responsible for any errors or omissions in this *Accepted Manuscript* or any consequences arising from the use of any information it contains.

# Structural and electronic properties of organo-halide hybrid perovskites from *ab initio* molecular dynamics

Claudio Quarti, Edoardo Mosconi, Filippo De Angelis\*

Computational Laboratory for Hybrid/Organic Photovoltaics (CLHYO), CNR-ISTM,

Via Elce di Sotto 8, I-06123, Perugia, Italy

\*e-mail: [filippo@thch.unipg.it](mailto:filippo@thch.unipg.it)

## Abstract

The last two years have seen the unprecedentedly rapid emergence of a new class of solar cells, based on hybrid organic-inorganic halide perovskites. The success of this class of materials is due to their outstanding photoelectrochemical properties coupled to their low cost, mainly solution-based, fabrication techniques. Solution processed materials are however often characterized by an inherent flexible structure, which is hardly mapped into a single local minimum energy structure. In this perspective, we report on the interplay of structural and electronic properties in hybrid lead iodide perovskites investigated by *ab-initio* molecular dynamics (AIMD) simulations, which allow the dynamical simulation of disordered systems at finite temperature. We compare the prototypical MAPbI<sub>3</sub> (MA=methylammonium) perovskite in its cubic and tetragonal structure with the trigonal phase of FAPbI<sub>3</sub> (FA=formamidinium), investigating different starting arrangements of the organic cations. Despite the relatively short time scale amenable to AIMD, typically a few tens of ps, this analysis demonstrates the sizable structural flexibility of this class of materials, showing that the instantaneous structure could significantly differ from the time and thermal averaged structure. We also highlight the importance of the organic-inorganic interactions in determining the fluxional properties of this class of materials. A peculiar spatial localization of the valence and conduction band edges is also found, with a dynamics in 0.1 ps range of, which is associated to the positional dynamics of the organic cations within the cubo-octahedral perovskite cage. This asymmetry in the spatial localization of the band edges is expected to ease exciton dissociation and assist the initial stages of charge separation, possibly constituting one of the key factors for the impressive photovoltaic performances of hybrid lead-iodide perovskites.

## 1. Introduction

The field of photovoltaics has recently witnessed the swift surge of a new class of solar cells based on mixed organo-halide lead perovskites. The unique properties of this class of materials allowed to attain impressive photovoltaic performances in just few years, at the point that hybrid perovskites have been claimed as the “*next big thing in photovoltaics*”.<sup>1</sup> Their first application in the field of photovoltaics was reported by Kojima et al. and it traces back only to 2009,<sup>2</sup> but the use of the lead-halide based compounds, like  $\text{KPbI}_3$ , in this field was already envisaged in the 1980s.<sup>3,4</sup> From the seminal work of Kojima et al.,<sup>2</sup> the interest towards hybrid lead halide perovskites increased exponentially, followed by an unprecedented boost in their photovoltaic performances. The use of  $\text{TiO}_2$  surface treatment before the perovskite deposition allowed Park et. al. to improve the power conversion efficiency (PCE) from the original 3.8% obtained by Kojima et al.<sup>2</sup> to 6.5%.<sup>5</sup> Subsequently, the use of the spiro-MeOTAD as solid state hole transporting material (HTM) allowed further improvements in both the stability and the PCE of organic-inorganic perovskite based-solar cells, reaching independently values of 9.7% and 10.2%, respectively.<sup>6,7</sup> The development of new cell structures and the improvement over the materials morphology control signed further steps forward the development of performing perovskite based devices, with PCE of 12.0% reported by Seok and coworkers,<sup>8</sup> 15% by Grätzel and coworkers,<sup>9</sup> and 15.4% by Snaith and coworkers.<sup>10</sup> This latter result, obtained with a planar heterojunction architecture, is of particular technological interest, paving the way for the production of stable and highly reproducible devices. The current PCE records in perovskite-based solar cell, 19.3% reported in the scientific literature<sup>11</sup> and a certified 20.1%,<sup>12</sup> make this new technology competitive with respect to other, long standing technologies, such as thin-film CdTe devices.<sup>13</sup>

Together with the impressive improvement in the materials synthesis techniques and in the device design, there has been a great effort to unveil the basics properties of this class of materials. Snaith and coworkers firstly demonstrated the capability of methylammonium lead-halide to act both as photon absorber and as electron transporting material.<sup>7</sup> The use of vibrational spectroscopy allowed to identify the markers of the crystalline order,<sup>14,15</sup> and to highlight the importance of the orientational dynamics of the methylammonium, MA, organic cation in the  $\text{CH}_3\text{NH}_3\text{PbI}_3$  perovskite (here on  $\text{MAPbI}_3$ ),<sup>16</sup> which is the most investigated organic-inorganic perovskite in photovoltaics. Time-resolved UV-vis absorption and photoluminescence measurements probed the micrometer diffusion length of the photo-generated species, in  $\text{CH}_3\text{NH}_3\text{PbI}_3$  ( $\text{MAPbI}_3$ ) and in its chlorine doped analogue,  $\text{CH}_3\text{NH}_3\text{PbI}_{3-x}\text{Cl}_x$  ( $\text{MAPbI}_{3-x}\text{Cl}_x$ ),<sup>17,18</sup> and demonstrated their inherent low charge

recombination rates.<sup>19</sup> Further studies by Petrozza et. al. finally established the nature of the photo-generated species, demonstrating that free electrons and holes are the main photo-generated species in MAPbI<sub>3-x</sub>Cl<sub>x</sub> perovskite in the typical photovoltaic working conditions.<sup>20</sup> Hodes et al. have further demonstrated the ambipolar response of the photoactive perovskite layer within the solar cell, with carriers generated on the hole transporting and electron transporting perovskite interfaces.<sup>21,22</sup>

Theoretical simulations have assumed a crucial role in the fundamental understanding of hybrid-organo halide perovskites. The unexpected agreement of the standard DFT predicted band gap with experiments<sup>23,24</sup> highlighted the role of both relativistic and electronic correlation effects. Mosconi et al. suggested the possibility that such agreement is merely fortuitous, due to an error cancellation between contributions from electronic correlation and spin-orbit-coupling (SOC).<sup>24</sup> A giant spin-orbit coupling effect was indeed reported by Even et al., which led to the expected underestimate of the SOC-DFT calculated band-gap.<sup>25</sup> State-of-the-art SOC-GW calculations have then delivered improved band-gap values, confirming the importance of SOC and correlation effects.<sup>26,27</sup> Recently, Menendez Proupin et al. also confirmed the importance of the subtle balance between electronic correlation and SOC, based on hybrid DFT calculations.<sup>28</sup> The introduction of relativistic SOC contributions in DFT calculations pointed out also very peculiar features of the band structure of hybrid lead-halide perovskites, as the Rashba/Dresselhaus effect, i.e. a splitting in the momentum space of the spin bands.<sup>26,28,29</sup> The specific role of the Rashba/Dresselhaus splitting on their photovoltaic working mechanism of the hybrid perovskite is still to be clarified, but the presence of two decoupled spin channels could provide opportunities to exploit the spin and orbital degrees of freedom in the photoinduced effect of photovoltaics.<sup>29</sup>

Electronic structure calculations have been also at the basis of the analysis of the claimed ferroelectric properties of MAPbI<sub>3</sub>. A permanent polarization of the MAPbI<sub>3</sub> in the tetragonal  $\beta$ -phase under an external electric field has been reported by Stoupos et. al.,<sup>30</sup> and also the presence of  $\sim 100$  nm size ferroelectric domains in MAPbI<sub>3</sub> has been observed.<sup>31</sup> However, contributions from ferroelectricity to the photovoltaics working mechanisms of this class of materials were not conclusively demonstrated.<sup>31</sup> A theoretical estimate of  $38 \mu\text{C}/\text{cm}^2$  for the polarization of the MAPbI<sub>3</sub> perovskites has been provided by Frost et al. from DFT calculations,<sup>32</sup> a value in the same order of magnitude of traditional ferroelectric oxides. Other research groups have however provided much smaller polarization values for MAPbI<sub>3</sub>,  $\sim 4 \mu\text{C}/\text{cm}^2$ ,<sup>33,34</sup> as well as for the CH(NH<sub>2</sub>)<sub>2</sub>SnI<sub>3</sub> perovskite (here on FASnI<sub>3</sub>),  $\sim 5 \mu\text{C}/\text{cm}^2$ .<sup>35</sup> All these results thus suggest a potentially reduced role of

ferroelectricity on the photovoltaic properties of this class of materials. As a matter of fact, we recently reported that despite a (mild) ferroelectric phase is the most stable structure for MAPbI<sub>3</sub> at zero temperature, disordered structures lay just 0.02 eV higher per unit formula,<sup>33</sup> thus being accessible at room temperature. Theoretical simulations have also been fundamental to study other basic aspects of hybrid halide perovskites, as the role of the MA cation,<sup>33,37,38,39</sup> the role of the MAPbI<sub>3</sub> and TiO<sub>2</sub> interface,<sup>40,41</sup> the transport properties,<sup>26,42,43,44</sup> the energetics of defects,<sup>45,46</sup> and the role of van der Waals interactions.<sup>47,48,49</sup>

One of the main advantages of this class of materials is the possibility to resort to low cost, solution synthesis techniques, paving the way for the production of low cost perovskite-based devices. On the other hand, solution processed materials generally have an inherently “*soft*” structure. For instance, the orientational dynamics of the MA cation in the cubo-octahedra cavity of MAPbI<sub>3</sub> has been long time pointed out in the literature.<sup>50,51</sup> In this regard, the description of this class of materials should be able to account for this inherent structural flexibility. Ab-initio molecular dynamics (AIMD) represent an interesting simulation tool in this sense, since they directly consider the structural flexibility of the material retaining a first principles description of their electronic structure. In addition, AIMD tools allow researchers to simulate the material in conditions closer to the operative one, i.e. at finite and varying temperature or pressure. To the best of our knowledge, only four molecular dynamics investigations have been reported in the literature on hybrid metal-halide perovskites, three in the high temperature cubic  $\alpha$ -phase,<sup>16,37,52</sup> and one in the room temperature tetragonal  $\beta$ -phase of the prototypical MAPbI<sub>3</sub>.<sup>33</sup>

In this perspective, we wish to provide a unified view of recent results from previous Car-Parrinello molecular dynamics simulations, carried out on the  $\alpha$ -phase,<sup>16</sup> and on the  $\beta$ -phase of the MAPbI<sub>3</sub>.<sup>33</sup> Besides, we report the results from additional AIMD simulations on the  $\beta$ -phase of the MAPbI<sub>3</sub> and on the  $\alpha$ -phase of the CH(NH<sub>2</sub>)<sub>2</sub>PbI<sub>3</sub> perovskite, hereafter FAPbI<sub>3</sub>. Here, we focus on the large structural flexibility of hybrid lead iodide perovskites in relation to: *i*) the different crystallographic structure (cubic/tetragonal); *ii*) the effect of different organic cations (MA vs. FA); and *iii*) the different starting orientation of the organic cations. In addition we demonstrate that the ion dynamics of this class of materials results in the localization of the valence and conduction electronic states, which is expected to facilitate charge separation and to reduce carrier recombination.

The manuscript is organized as follows. In the Section 2, we detail the structural models and computational methods employed. In the Section 3.1, we discuss the structural features of the MAPbI<sub>3</sub>

and FAPbI<sub>3</sub> perovskites. In the Section 3.2, we focus on the electronic properties of these materials. In the Section 4, we summarize our results, in relation with their implications in the photovoltaic field.

## 2. Models and methods

We investigate the cubic,  $\alpha$ -phase and the tetragonal,  $\beta$ -phase of the MAPbI<sub>3</sub> hybrid perovskite, resorting to the models reported in Ref. 16 and Ref. 33 for these two phases, respectively. An additional structural model for the  $\beta$ -phase of MAPbI<sub>3</sub> and for the  $\alpha$ -phase of FAPbI<sub>3</sub> are presented here for the first time. All the investigated structural models are depicted in Figure 1. The  $\beta$ -phase of the MAPbI<sub>3</sub> is simulated by a 2x2x2 tetragonal supercell, and it contains 32 MAPbI<sub>3</sub> chemical units. While there are claims that this supercell may be insufficient to capture the long range disorder of the MA cations, still it should be reasonable for qualitative comparisons. The cell parameters are fixed at twice the experimental value from the values by Poglitsch and Weber ( $a=b=17.7112$  Å,  $c=25.32$  Å).<sup>50</sup> Here, we use the two models reported in Ref. 33, named MA  $\beta$ 1 and MA  $\beta$ 3, and an additional new structure, named MA  $\beta$ 2. These three structures differ in the starting orientation of the MA cations. MA  $\beta$ 1, is characterized by an isotropic orientation of the MA cations within the  $ab$ -plane, and an anisotropic orientation with respect to the  $c$ -axis, with the MA cations tilted by  $\sim 30^\circ$  with respect to the  $ab$ -plane. The present model shows a polarization along the  $c$ -axis of  $4.41 \mu\text{C}/\text{cm}^2$ .<sup>33</sup> The  $\beta$ 2 and  $\beta$ 3 model show an isotropic distribution of the MA cations both with respect to the  $ab$ -plane and along the  $c$ -axis and there are thus paraelectric. The  $\beta$ 2 structure possesses a symmetry plane at half of the  $c$  cell parameter, with the MA cations lying upper/lower such a plane that have the nitrogen atoms pointing down/up. In other words, the  $\beta$ 2 is globally paraelectric but it has two domains with opposite orientation of the MA cations (see Figure 1). The  $\beta$ 3 instead is both locally and globally paraelectric.

The  $\alpha$ -phase of MAPbI<sub>3</sub>, here-on named MA $\alpha$ , is simulated using a 2x2x2 cubic supercell and it contains 8 MAPbI<sub>3</sub> chemical units. The cell parameter was fixed to twice the experimental value by Poglitsch (12.66 Å),<sup>50</sup> and the initial orientation of the 8 MA cations was along the [111] direction. Finally, the  $\alpha$ -phase of the FAPbI<sub>3</sub>, here on FA $\alpha$ , is simulated with a 2x2x2 supercell of the XRD experimental trigonal structure from Ref. 30, with the cell parameters doubled with respect to the experimental parameters ( $a=b=17.9634$  Å,  $c=22.012$  Å). The  $\alpha$ -FAPbI<sub>3</sub> structure reported by Stoumpos et. al. does not show the typical octahedral tilting found for instance in the  $\beta$ -MAPbI<sub>3</sub>, thus being more similar to a cubic structure. For this reason, we will refer to the  $\alpha$ -FAPbI<sub>3</sub> as “pseudo-cubic”.

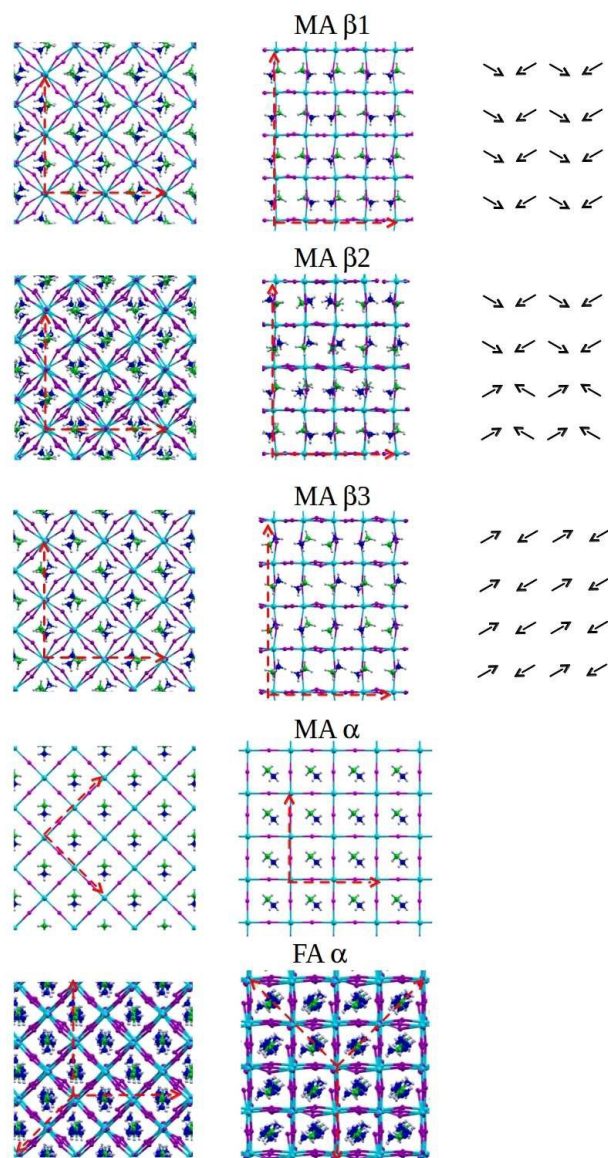


**Figure 1.** Top view and side view of the structural models for the  $\text{MAPbI}_3$  and  $\text{FAPbI}_3$ : the tetragonal  $\beta$ -phase of  $\text{MAPbI}_3$  (MA  $\beta_{1,2,3}$ ) and the cubic- $\alpha$  phase of  $\text{MAPbI}_3$  (MA  $\alpha$ ) and the triclinic, pseudo-cubic - $\alpha$  phase of  $\text{FAPbI}_3$  (FA  $\alpha$ ). For the tetragonal MA  $\beta_{1,2,3}$  structures, we report also the starting orientation of the MA cations. The red-arrows represents the cell parameters.

Car-Parrinello molecular dynamics<sup>53</sup> simulations have been performed on all these structures, as implemented in the Quantum-Espresso package.<sup>54</sup> All calculations are performed with PBE exchange-correlation functional,<sup>55</sup> along with scalar-relativistic (SR), ultrasoft<sup>56</sup> pseudopotentials and a 25/200 Ry cutoff for wavefunction/density plane wave expansion. A time step of 5 a. u., electronic mass of 400 a.u. and real ionic masses have been used, except for the hydrogen that has been deuterated. For MA $\alpha$ ,

a time step of 4 a.u. was used and all the ionic masses are real. All the simulations, except the MA $\alpha$ , are conducted at 350 K without constraints. The simulation on the MA $\alpha$  system has been carried out at 319 K. To avoid possible phase transitions to the room temperature stable tetragonal  $\beta$ -phase, that takes place at 327 K, we have fixed the lead atoms in their cubic sites. For more details regarding the assumptions introduced for MA $\alpha$ , we refer to Ref. 16. In all cases, the simulation time was at least 12 ps, after a few picoseconds of thermalization.

The importance of spin-orbit coupling on the electronic properties of this class of materials has been already highlighted in the literature,<sup>24-28</sup> but its impact on the structural properties has also been shown to be relatively small with comparable equilibrium geometries calculated by SR- and SOC-DFT.<sup>26</sup> This justifies the use of SR-DFT as the electronic structure basis for AIMD simulations.

We also notice that our as well as previously reported AIMD simulations do not include van der Waals interactions. While van der Waals interactions may surely affect the dynamics of organo-halide perovskites (as any other change in the interaction potential would do) we previously showed that they do not affect neither the shape of the crystalline cell of MAPbI<sub>3</sub> (i.e. the  $c/a$  ratio) nor the energetics with respect to the cations orientation.<sup>33</sup> Since here we mainly compare the properties of similar materials, we believe the present level of theory to be sufficient for their qualitatively homogeneous description.

### 3. Results and Discussion

#### 3.1 Structure and dynamics of MAPbI<sub>3</sub> and FAPbI<sub>3</sub> perovskites

An in-depth understanding of the structure of hybrid lead halide perovskites requires the use of different experimental techniques, probing different spatial scales, from the crystal grains to the local octahedral distortion, and the inherent dynamics of the structure. To the best of the authors' knowledge, the structure of this class of materials has been investigated mainly through X-ray diffraction (XRD) measurements,<sup>30,50,57,58,59</sup> but such a technique is informative only of the static (long time scale), long range order of the material and it provides limited indications of the local order or on the structure dynamics. Few vibrational spectroscopic investigations have been reported in the literature, pointing out the different time-scale of the inorganic framework dynamics (below 100 cm<sup>-1</sup>), of the librations of the MA cations (below 200 cm<sup>-1</sup>) and of the internal vibrations of the MA cations (above 300 cm<sup>-1</sup>).<sup>14-16</sup> Also the analysis of the radial distribution function (RDF) of specific atomic species, obtained from X-ray diffraction, was particularly useful to unveil the inherent local disorder of

hybrid metal halide perovskites.<sup>59,60</sup> In Figure 2, we report the RDF, obtained from our AIMD simulations, associated to the inorganic framework of the investigated structures. The theoretical data for the  $\beta$ -phase of MAPbI<sub>3</sub> is also compared with the available experimental data,<sup>59</sup> while the RDF of the MA $\alpha$  and FA $\alpha$  are reported for sake of comparison. The general agreement between theory and experiment for the  $\beta$ -MAPbI<sub>3</sub> is quite good, especially for the  $\beta$ 1 model. A very small signal at  $\sim 5.5$  Å is found experimentally, which is not paralleled by theoretical calculations. It is worth to mention however that the analysis of the experimental RDF from Ref. 59 pointed out the presence of a significant fraction of disordered domains ( $\sim 70\%$ ) in the sample. Thus, the fact that such signal is not found in the periodic crystalline model is consistent with its assignment to spatial disorder. Notice that the most stable among our calculated MAPbI<sub>3</sub> structures, i.e. MA  $\beta$ 1,<sup>16</sup> closely resembles the most recently reported experimental structure found at 180 K,<sup>61</sup> showing also a similar optimized cell shape to the experimental one.<sup>33</sup> This suggests the calculated MA  $\beta$ 1 structure to be associated to the low-temperature, partly ordered, MAPbI<sub>3</sub> phase of Ref. 61.

We observe that the different starting orientation of the MA cations for the MA  $\beta$ 1,2 and 3 structures (see Figure 2) results in a different broadening and relative height of the peaks in the RDF, thus demonstrating that the structure and the dynamics of the inorganic framework is not decoupled from the organic component, as discussed in a previous work.<sup>16</sup> The peaks in the RDF become broader going from the  $\beta$ 1 to  $\beta$ 2 and  $\beta$ 3 structure, with a larger broadening that can be addressed to a smaller degree of long-range order (static disorder) and/or to a less “rigid” structure (dynamic disorder). Note that static techniques, as the XRD, are quite insensitive to the orientation of the MA cations and on their effects on the structure of the inorganic component. In fact, in Figure SII, we show that the theoretical XRD patterns computed on the average structures over the whole simulation time (12 ps) for the MA  $\beta$ 1,2 and 3 structures are almost the same, differing in very weak signals which are not resolved in the experimental data

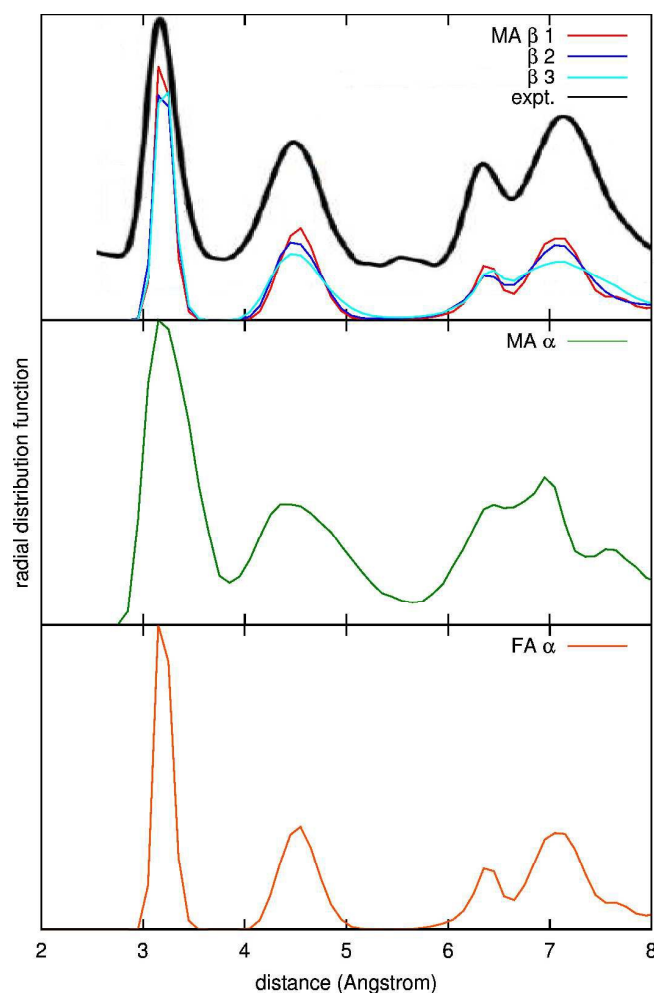


**Figure 2.** Radial distribution function (RDF) associated to the inorganic framework of  $\text{MAPbI}_3$  and  $\text{FAPbI}_3$ , obtained from CP simulations; upper panel) RDF of three structural models for the tetragonal MA  $\beta 1$ ,  $\beta 2$  and  $\beta 3$ , characterized by a different starting orientation of the MA cations, compared with the experiment. The theoretical intensity is normalized with respect to the intensity of the I-I peak at 4.5 Å; central panel) theoretical RDF for the cubic,  $\text{MA}\alpha$  perovskite; lower panel) theoretical RDF of the cubic,  $\text{FA}\alpha$ . Experimental RDF from Ref. 59, adapted with permission from J. J. Choi, X. Yang, Z. M. Norman, S. J. L. Billinge and J. S. Owen, Structure of Methylammonium Lead Iodide Within Mesoporous Titanium Dioxide: Active Material in High Performance Perovskite Solar Cells, *Nano Lett.* 2014, 14, 127-133. Copyright 2013, American Chemical Society.

Moving to the  $\alpha$ - $\text{MAPbI}_3$  phase, we found much broader peaks and a general different shape of the RDF at a distance larger than 6 Å, as expected from the different crystal structure. The larger broadening of the RDF in the case of the  $\alpha$ - $\text{MAPbI}_3$  is clearly associated to the inherent larger disorder

of this phase, consistently with the fact that such a phase is stable at high temperature; on the other hand, we will show that such behavior is also connected to a much faster rotational dynamics of the MA cations (see Section 3.2). Finally, the RDF calculated for the FA $\alpha$  phase resembles that of the  $\beta$ -MAPbI<sub>3</sub> models rather than that of the MA $\alpha$  phase, despite the different crystalline structure.

One of the main advantages of molecular dynamic simulations relies on the possibility to follow the value of specific structural variables and of its evolution in time, thus obtaining a deeper description of the system under investigation. One of the most important structural parameters, that determines the final crystalline structure of perovskite ABX<sub>3</sub> is the rotation or titling of the BX<sub>6</sub> octahedra along the pseudo-cubic axes, as discussed by Glazer.<sup>62</sup> A fully cubic structure is characterized by null rotations of the PbI<sub>6</sub> octahedra, or by a  $a^0a^0a^0$  structure in the Glazer notation. In other words, the I-Pb-Pb-I dihedral angles measured along each of the three pseudo-cubic axes are zero, as schematically depicted in the Figure 3a. The tetragonal,  $\beta$ -phase of MAPbI<sub>3</sub> is instead characterized by an “out-of-phase” rotation of the PbI<sub>6</sub> octahedra along the  $c$ -axis,<sup>30,57</sup> or by a  $a^0a^0c^-$  structure in the Glazer notation,<sup>62</sup> as depicted in Figure 3b. Such structure results in alternating positive and negative I-Pb-Pb-I dihedral angles along the  $c$ -axis. For the investigated structures, we have followed the evolution of all the I-Pb-Pb-I dihedral angles within the simulation cell (in Figure SI2, we report their average, without sign, along the three pseudo-cubic axes). In Figure 3c, we have plotted the distributions of the I-Pb-Pb-I dihedral angles along the three pseudo-cubic axes, as obtained from our AIMD simulations. The main difference of the tetragonal MA  $\beta$ 1,2,3 with respect to the cubic MA $\alpha$  and pseudo-cubic FA $\alpha$  structures is found along the [001] directions, as expected from the aforementioned octahedral rotation. For the MA $\alpha$  and FA $\alpha$  structures, the distributions along [001] have a maximum for a value of the dihedral I-Pb-Pb-I angle of 0° and it oscillates mainly between  $\pm 20^\circ$ . At the opposite, the distribution of the dihedral angles for the tetragonal MA  $\beta$ 1,2,3 along [001] show two maxima at  $\pm 30^\circ$ , corresponding to the “out-of-phase” rotation of the octahedra along the [001] direction. Note that such a value of the I-Pb-Pb-I dihedral angle is partly overestimated with respect to the experimental values from Kawamura et al., 21°,<sup>57</sup> and from Stoumpos et al., 16°.<sup>30</sup> However, such a behavior was found also for static DFT calculations, thus the tilting overestimation is probably inherent to the employed electronic structure method<sup>63</sup> or it could be a consequence of the short simulation times which may not allow a full thermalization of the slow atomic motion components.

Focusing on the tetragonal structure, we found two important results. First, also for the “more rigid” MA  $\beta$ 1 structure, all the distributions show a broadening of the order of 20° along the [110],

[1-10], and  $10^\circ$  along the [001] direction, thus pointing to a certain degree of structural flexibility for this class of materials. Second, for the MA  $\beta 3$  structure the distributions of the dihedral angles along the [110] and [1-10] show two distinct maxima around  $\pm 10^\circ$ , thus demonstrating that MA  $\beta 3$  is characterized by a  $a^-b^-c^-$  structure, different from the  $a^0a^0c^-$  structure proposed for the MAPbI<sub>3</sub> perovskite.<sup>30,58</sup> On the other hand, previous static DFT calculations showed that the MA  $\beta 3$  structure is less stable than the MA  $\beta 1$ , by only 0.02 eV per formula unit.<sup>33</sup> It is therefore possible that at room temperature the most stable,  $a^0a^0c^-$  structure (MA  $\beta 1$ ) evolves to the less stable  $a^-b^-c^-$  structure, as consequence of a various random reorientations of the MA cations, which take place in the picoseconds time-scale.<sup>50,51</sup> Then, the system remains in such distorted structure, as long as various rotations of the MA cations bring it back to the more stable  $a^0a^0c^-$  like structure (MA  $\beta 1$ ). This result however demonstrates that the actual structure of the MAPbI<sub>3</sub> perovskite can deviate significantly from the nominal  $a^0a^0c^-$  structure, highlighted from XRD measurements.

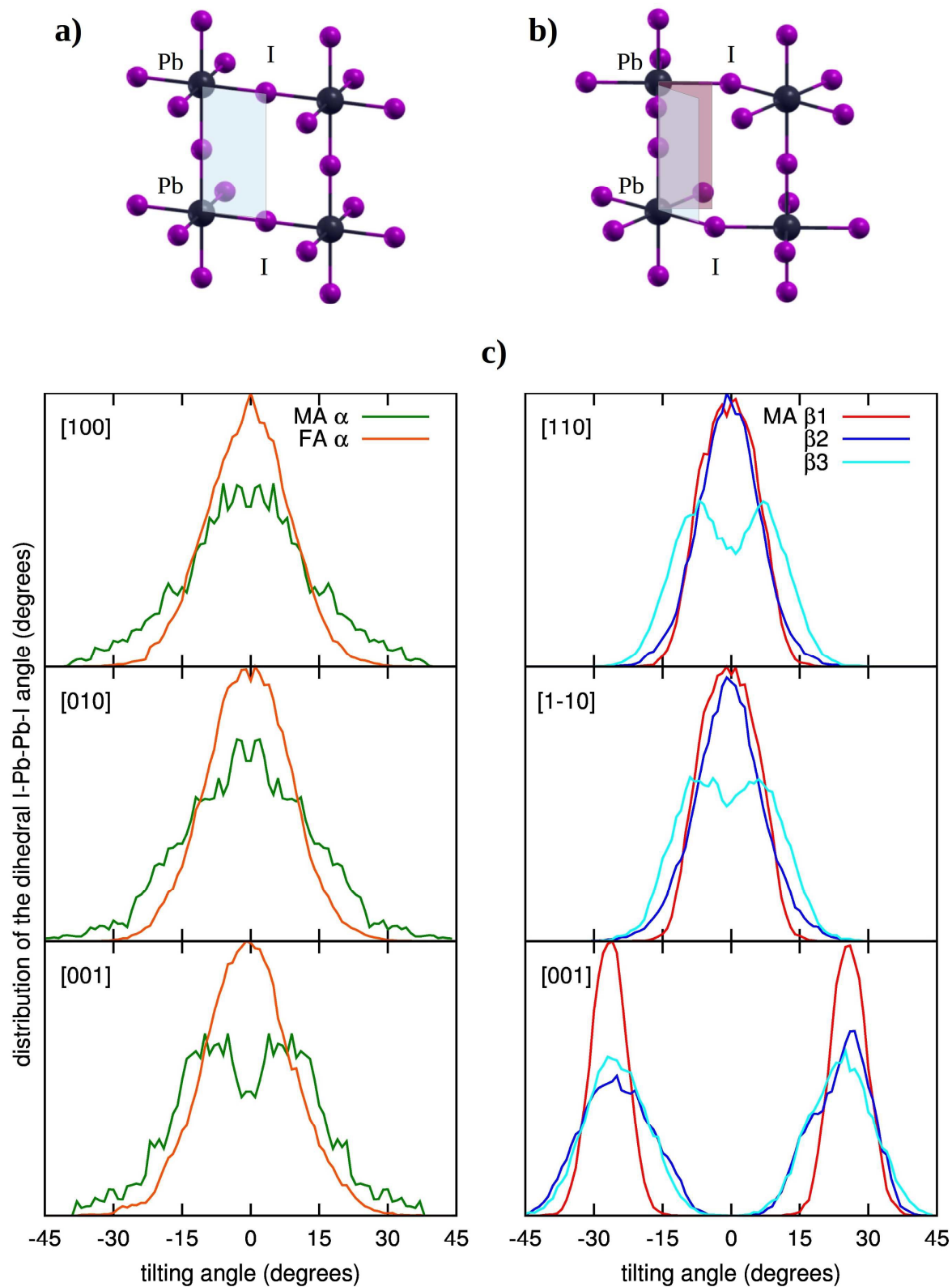


**Figure 3.** a) I-Pb-Pb-I dihedral angle for a cubic crystal, characterized by a null rotation of the  $\text{PbI}_6$

octahedra ( $a^0a^0a^0$  in the Glazer notation); <sup>62</sup> b) I-Pb-Pb-I dihedral angle for a tetragonal crystal, characterized by an “*out-of-phase*” rotation of the  $\text{PbI}_6$  octahedra along the  $c$ -axis ( $a^0a^0c^-$  in the Glazer notation); <sup>62</sup> c) distribution of the values assumed by all the I-Pb-Pb-I dihedral angles within the cell during the AIMD simulations, for the  $\text{MA } \alpha$  and  $\text{FA } \alpha$  structures (left panel) and the  $\text{MA } \beta_{1,2,3}$ , (right panel). The distributions are reported for the crystallographic directions corresponding to the pseudo-cubic axes.

From Figure 3, we also observe also that the  $\text{MA } \alpha$  and  $\text{FA } \alpha$  structures show a broader distribution of the I-Pb-Pb-I angles with respect to the tetragonal structures, thus pointing to a larger flexibility for cubic and pseudo-cubic structures. We also observe that the  $\text{MA } \alpha$  structure still shows a splitting of the dihedral angle distribution along  $[001]$ , as in the case of the tetragonal structures, although to a much smaller extent. This behavior could be a signature of the initial stages of a cubic  $\rightarrow$  tetragonal phase transition (our simulations on the  $\text{MA } \alpha$  structure are carried out at the edge of the phase transition temperature). However, it is worth to note that for  $\text{MA } \alpha$  a constraint on the motion of the lead atoms was imposed, fixing them to the cubic sites; thus, it is difficult to assess whether such peculiar feature is specific of the  $\alpha$ - $\text{MAPbI}_3$  over the  $\alpha$ - $\text{FAPbI}_3$  or if it is due to this constraint.

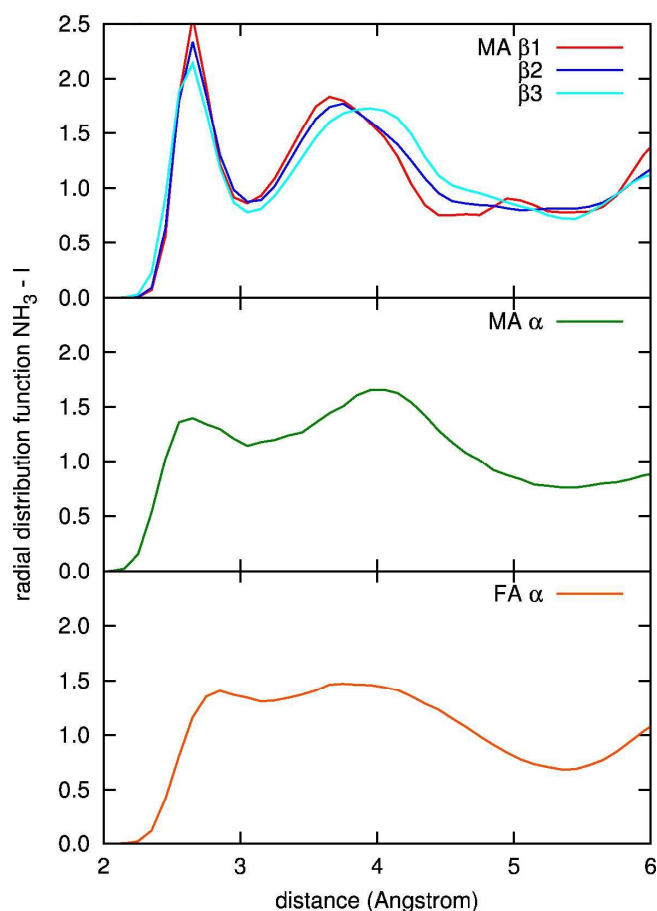


**Figure 4.** Radial distribution function of the hydrogen atoms of the ammonium group and the iodine atoms for the five investigated structures: MA  $\beta$ 1,2,3 (top panel), MA  $\alpha$  (central panel) and FA $\alpha$  (lower panel).

Hybrid organic-inorganic perovskites ABX<sub>3</sub> are characterized by the presence of an organic cation in the site A, which interacts with the inorganic framework mainly through hydrogen bonds. As a result, the organic cations are free to rotate within the cubo-octahedral cavity, and their dynamics is obviously determined by available thermal energy, the reciprocal size of the cation and the cubo-octahedral cavity and the strength of the specific organic-inorganic interactions. In Figure 4, we report the radial distribution function (RDF) associated to the distances between the iodine atoms and the nitrogen-bound hydrogen atoms, that is informative of the formation of hydrogen bonds between the organic cations and the inorganic framework. The calculated RDFs are significantly different in the case of the tetragonal and (pseudo)cubic structures. The tetragonal structures show a well defined peak at 2.65 Å, corresponding to NH<sub>3</sub><sup>+</sup>-I hydrogen bonds. On average, the number of NH<sub>3</sub><sup>+</sup>-I hydrogen bonds during the AIMD simulation is 2.5 for MA  $\beta$ 1 and it decreases to 2.3 to 2.1, going from MA  $\beta$ 2 and to MA  $\beta$ 3. Together, we observe a general broadening of the first peak going from the MA  $\beta$ 1 to MA  $\beta$ 2 to MA  $\beta$ 3 structure. In the case of the MA $\alpha$  and the FA $\alpha$  structures, we still observe the peak at 2.65 Å but it reduces to less than 1.5 hydrogen bonds, on the average.

**Table 1.** Statistical analysis of the orientations of the organic cations, for MA  $\beta$ 1,2,3, MA  $\alpha$  and FA $\alpha$ . The average (av.), standard deviation (st. dev.) and the range of values of  $\theta$  and  $\varphi$  assumed by the MA/FA cations are reported, averaged on all number of MA/FA cations and over the whole simulation time. Data are in degrees.

	$\theta$			$\varphi$		
	av.	st. dev.	range	av.	st. dev.	range
tetragonal						
MA $\beta$ 1	180	8	57	-26	6	53
$\beta$ 2	136	10	55	1	7	49
$\beta$ 3	177	16	89	-2	9	55
cubic						
MA $\alpha$	163	65	349	-26	32	132
FA $\alpha$	177	86	355	0	38	161

Now, we show that such a difference in the organic-inorganic interactions, going from the cubic to the tetragonal phase is reflected in a different dynamics or the rotations for the organic cations. We followed the orientation of CN/CH bond associated to each MA/FA cation and we described it by using the Tait-Bryan angles,  $\theta$  and  $\varphi$  (see Figure 5a), as in our previous works.<sup>16,33</sup> The  $\theta$  angle describes the orientation of the CN/CH vector within the  $ab$ -plane and it assumes values between 0 and 360°, with 0° corresponding to the CN/CH vector aligned along the  $a$ -axis (see Figure 5a). The  $\varphi$  angle describes the tilting of the CN/CH vector with respect to the  $ab$ -plane and it is comprised between -90 and 90°, with 90° or -90° corresponding to the CN/CH vector aligned along or opposed to the  $c$ -axis and 0° corresponding to the CN/CH vector lying within the  $ab$ -plane (see Figure 5a). To summarize the orientational dynamics of the organic cations in the investigated systems, we performed a statistical analysis of the  $\theta$  and  $\varphi$  values assumed by the MA/FA cations during the AIMD simulations, see Table 1. The standard deviation and the range of values assumed by both  $\theta$  and  $\varphi$  are much larger in the cubic than in the tetragonal phase, with the MA/FA cations that explore nearly all the orientations within the  $ab$ -plane. In Figure 5b, we report the  $\theta$  and  $\varphi$  angles of a selected MA cation for the MA  $\beta$ 3, during the CPMD simulation. In the tetragonal phase, the MA cation jumps among specific configurations, which maximize the hydrogen bonding interactions,<sup>33</sup> in other words, in the tetragonal phase the MA cation goes through a simple re-orientational motion. At the opposite, in the cubic MA  $\alpha$  structure, the selected MA cation shows very fast rotations around 6 ps (see Figure SI3), in good agreement with the results from Knop et. al.,<sup>64</sup> that suggest a nearly free rotations on the MA cations in the cubic phase. Summarizing, the specific organic-inorganic interaction represents a fundamental feature in the tetragonal-cubic phase transition. In the tetragonal phase of the hybrid lead iodide perovskites, the thermal motion of the organic cations is hindered by the presence of a strong hydrogen-bond network. Going to the cubic phase, such hydrogen-bond network weakens and the MA cations are no more constrained along specific orientations, thus being free to rotate.

It is worth to mention that the short duration of our AIMD simulations (12 ps), with respect to the typical timescale of the rotational motion of the organic cations ( $\sim$ ps), does not allow us to provide accurate estimations of kinetic parameters associated to this motion, as relaxation<sup>50</sup> or correlation times.<sup>51</sup> On the other hand, a much longer simulation (58 ps) on the cubic phase of MAPbI<sub>3</sub> has been carried out by Frost et. al.<sup>37</sup>. Notably, also in this case, the authors pointed out that the simulation time may be too short to reach the complete coverage of the possible orientation of the MA cations, that

preserve in good part their initial  $\langle 100 \rangle$  orientation. In this regard, the use of classical dynamics simulations, allowing for much longer time scales to be probed, is highly desirable, to investigate the kinetic parameters associated to the cation rotation, in a statically meaningful time scale.

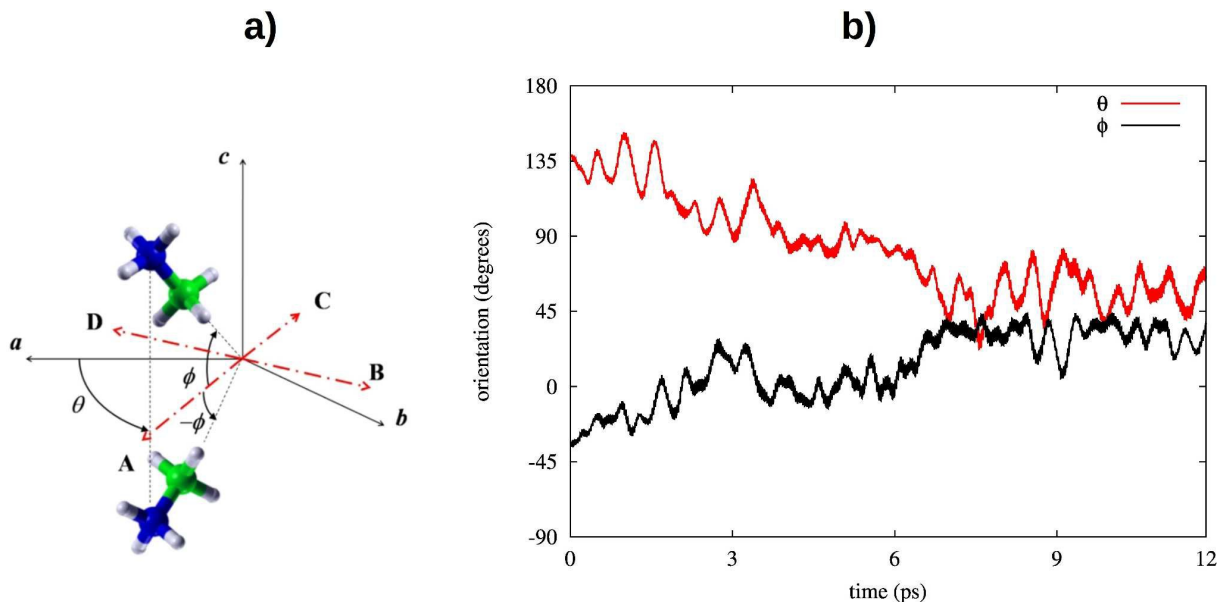


**Figure 5.** a) description of the orientation of the organic cation in  $\text{MAPbI}_3$  using the Tait-Bryan angles,  $\theta$  and  $\varphi$ ; b) time evolution of the orientation ( $\theta$  and  $\varphi$ ) of one of the rotating MA cations in MA  $\beta 3$ .

### 3.2 Dynamics and band-gap fluctuations.

As from previous works, it is clear that the nuclear dynamics may imply significant oscillations of the electronic energy levels of the  $\text{MAPbI}_3$  perovskite.<sup>16,33</sup> For the cubic phase of  $\text{MAPbI}_3$ , we found that the energy of the HOMO level varies within a range of  $\sim 0.5$  eV,<sup>16</sup> which is comparable to the variation in the electronic properties typically found for organic semiconductors and dye-sensitized interfaces.<sup>63</sup> In a subsequent paper on the tetragonal phase of the  $\text{MAPbI}_3$ , we reported a strongly reduced variation of the HOMO level, within a range of  $\sim 0.1$  eV, for the structure corresponding to the current MA  $\beta 1$ .<sup>33</sup> In this Section, we treat more in the detail the effect of the ion dynamics on the electronic properties of hybrid organo-lead-halide perovskites. Here, we evaluate the variation of the band gap for the MA  $\beta 1$ , MA  $\beta 2$ , MA  $\beta 3$  structures and the FA  $\alpha$  structure. We exclude the MA  $\alpha$  structure from this discussion, because of the constrain on the lead atoms used in this simulation. In this way, the variation of the electronic properties is evaluated on the same ground:  $\sim 330$  K average temperature and no geometrical constrains. For the MA  $\beta 1$ , MA  $\beta 2$ , MA  $\beta 3$  and FA  $\alpha$  structures, we selected 200 geometries over the

whole dynamics (one geometry each  $\sim 0.06$  ps) and we performed a single point calculation to determine the HOMO-LUMO band gap, at the same theoretical level of the AIMD simulations. For the MA  $\beta 2$  and FA  $\alpha$  structures, we performed single point calculations also at the SOC-DFT level, thus considering also spin orbit coupling effects. We have previously showed that the electronic SOC-DFT band gap is more sensitive with respect to SR-DFT band gap to the octahedral tilting, as defined in the Figure 3a,b.<sup>63</sup> Thus, it is reasonable to find larger oscillations of the electronic levels at the SOC-DFT level of theory.

The variation of the band gap at the SR-DFT level for the four investigated structures is reported in Figure 6, while a statistical analysis of the results is summarized in the Table 2. The average band gap calculated at the SR-DFT level for the MA  $\beta 1$  (1.66 eV) and MA  $\beta 2$  (1.62 eV) is in good agreement with the experimental data the literature, ranging from 1.55 to 1.63 eV range.<sup>20,66,67,68</sup> The average band gap of MA  $\beta 3$  (1.79 eV) and of the FA  $\alpha$  (1.75 eV) instead are slightly overestimated with respect to the experiments (we recall that the experimental band gap of the  $\alpha$ -FAPbI<sub>3</sub> is 1.48 eV).<sup>30,69</sup> On the other hand, it is well known that the agreement between the SR-DFT band gap with the experiment is fortuitous and it is due to a cancellation of the contributions from electronic correlation and spin-orbit-coupling.<sup>25,26</sup> In fact, the average SOC-DFT band gap of the MA  $\beta 2$  and FA  $\alpha$  phases is underestimated by  $\sim 1$  eV.

The MA  $\beta 1$  structure shows the narrowest variation of the band gap among the investigated structures, within only 0.07 eV, as reflected by the smallest structural variations during the dynamics, i.e. by the narrower oscillation of the I-Pb-Pb-I dihedral angle and the by less mobile organic cations (see Table 1). The band gap in MA  $\beta 2$  and MA  $\beta 3$  instead shows a wider variation, within 0.20 and 0.15 eV respectively, consistently with the wider variation of both the I-Pb-Pb-I dihedral angles (see Figure 3c) and MA cations orientations (see Table 1). In this regard, it is difficult to disentangle the specific contributions from the inorganic component, i.e. to the band gap variations due to the oscillation of the I-Pb-Pb-I dihedral angle, or to the rotational motion of the organic cations. Further work is ongoing in this direction. Finally, the band gap in the FA $\alpha$  structure, for which full rotations of the organic FA cations are found, shows the largest variations, within 0.20 eV. Summarizing, in the present work, we estimate a variation of the band gap in hybrid lead-halide perovskites between 0.07 eV and 0.20 eV, in between with respect to our previous estimations in Ref. 16 and in Ref. 33 (0.46 and 0.07 eV global oscillation of the HOMO level during the dynamics). Thus, the variation of the electronic energy levels in this class of material is smaller, but still comparable to the typical variations

found for organic semiconductors and dye-sensitized interfaces ( $\sim 0.4$  eV).

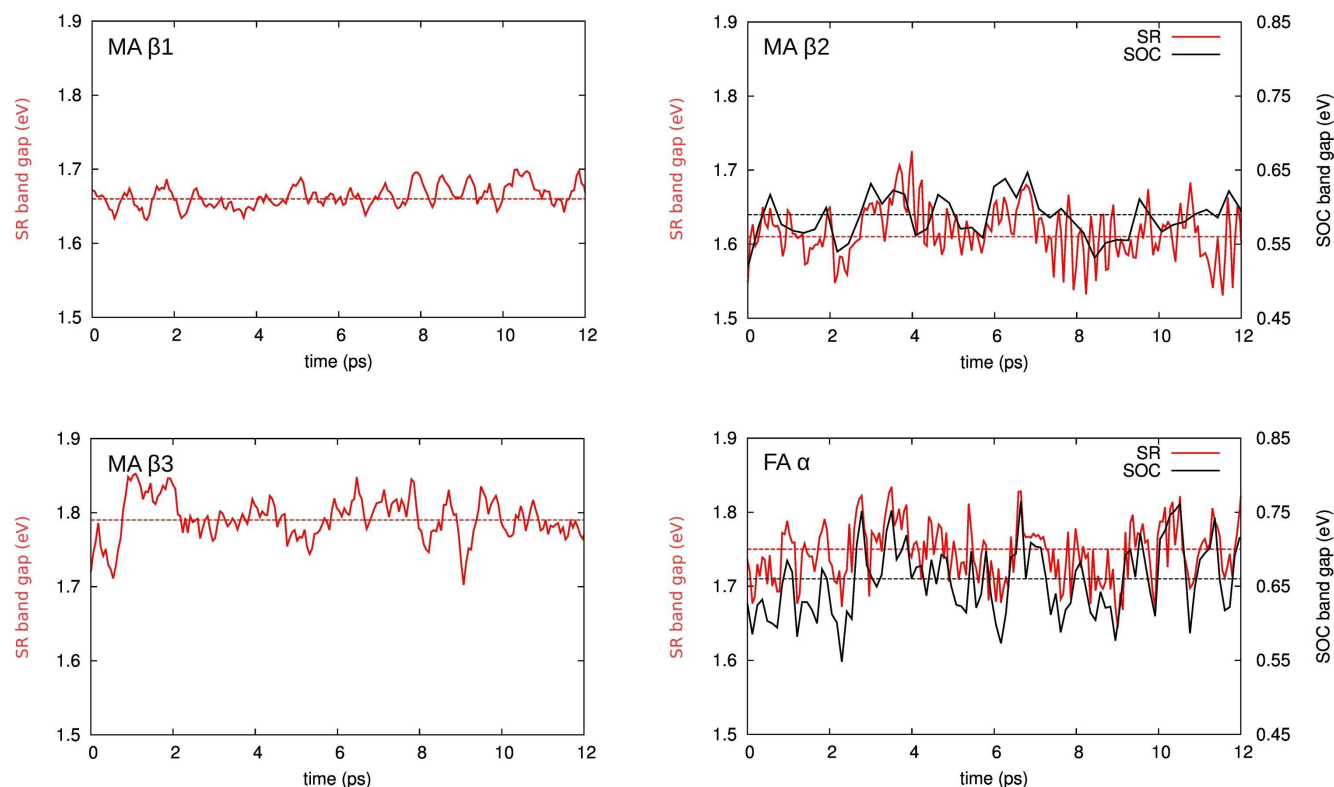


**Figure 6.** Evolution of the band gap during the CPMD simulations, for the tetragonal MA  $\beta 1,2$  and 3 and for the FA  $\alpha$  structure. SR- and SOC-DFT calculated band-gaps are reported in red and black colors, respectively.

**Table 2.** Average, standard deviation (st. dev.) and range of values (included with maximum and minimum values) assumed by the band gap during the molecular dynamics. The band gap is evaluated at the SR-DFT level for the MA  $\beta 1,2,3$  and FA  $\alpha$  structures and at the SOC-DFT for the MA  $\beta 2$  and FA  $\alpha$  structure. In parenthesis, the difference between the SOC-DFT value with respect to the SR-DFT one is reported. Data are in eV.

		average	st. dev.	Range	max	min
SR-DFT						
MA	$\beta 1$	1.66	$1.49 \times 10^{-2}$	0.07	1.70	1.63
	$\beta 2$	1.61	$3.51 \times 10^{-2}$	0.20	1.73	1.53
	$\beta 3$	1.79	$2.83 \times 10^{-2}$	0.15	1.85	1.70
FA	$\alpha$	1.75	$3.90 \times 10^{-2}$	0.20	1.84	1.64

		SOC-DFT				
MA	$\beta 2$	0.59	$2.94 \times 10^{-2}$ (-10%)	0.13 (-10%)	0.65	0.52
FA	$\alpha$	0.66	$4.79 \times 10^{-2}$ (+23%)	0.22 (+8%)	0.77	0.55

We now evaluate the contributions from spin-orbit-coupling on the band gap variations during the dynamics. As shown in Figure 6, for the MA  $\beta 2$  and the FA  $\alpha$  structures, the SOC-DFT band gap follows quite closely the SR-DFT band gap, apart from the aforementioned band gap underestimation at the SOC-DFT level. From Table 2, we observe two opposite trends in the pseudo-cubic FA  $\alpha$  and in the tetragonal MA  $\beta 2$  phase. In the former, we observe an increase in the band gap variation, as expected from the discussions from Ref. 63, while in the latter we observe a reduction in the band gap variation. The rationale behind the present results is the following. In Ref. 63, the band gap modulation with the increase of the I-Pb-Pb-I dihedral angle has been associated to a decrease of the Pb contribution to the conduction band, thus in a different covalency/ionicity of the Pb-I bond. Thus, in light of the main role of the lead atom, the spin-orbit coupling is essential to catch the correct band-gap variation with the nuclear dynamics. Figure 3c shows that in the tetragonal phase the I-Pb-Pb-I dihedral angle along [001] do not passes through zero, or, in other words, the structure never passes through a cubic-like structure. For this reason, the covalency/ionicity of the Pb-I bond does not changes significantly in this phase and thus the effect associated to SOC is expectedly small. In the cubic phase instead, since the I-Pb-Pb-I dihedral angle along [001] passes through zero (see Figure 3c), or, in other words, the structure oscillates from a cubic to a tetragonally distorted structure, with the character of the Pb-I bond oscillating from the “most ionic” (for I-Pb-Pb-I dihedral  $\rightarrow 0$ ) to “most covalent” (for dihedral angles  $\rightarrow \pm 30^\circ$ ). Concluding, the contribution from spin-orbit coupling effects on the band gap variation with the nuclear dynamics is larger in the cubic than in the tetragonal cell. On the other hand, also in the cubic phase, such contribution is limited to a maximum of 23% of the total variation.

Finally, we focus on the electronic Density of States (DOS) in correspondence of the valence band. Lindblad et. al.<sup>52</sup> already pointed out the role of the structural dynamics on the broadening of the valence band. In Figure SI4, we report the DOS calculated for the investigated structures. There is a general good agreement between our DOS and that obtained by Lindblad et. al.,<sup>52</sup> with a valence band that is spread over a similar range of energies that that found by Lindblad et al. and that found experimentally. It is interesting to note that our SOC-DFT calculations, carried out only on MA  $\beta 2$  and FA  $\alpha$ , predict a shape of the valence band in better agreement with the experiments with respect to the SR-DFT calculations, with the presence of two main maxima with an intensity ration of  $\sim 3/2$ . The good

agreement of the SOC-DFT DOS, obtained on the structures from molecular dynamics at the SR-DFT level confirms the reliability of the latter method to describe the structural dynamical features of hybrid perovskites.

### 3.3 Impact of nuclear dynamics on charge localization.

Finally, we investigated the localization of the electronic states during the nuclear dynamics, as follows. For all the structures, together with the band gap, we calculated also the density of states (DOS) and the contributions from all the atoms within the reference cell (pDOS). Then, for the  $\beta$ -phase of MAPbI<sub>3</sub> we estimated the delocalization of the frontier electronic states along [001] direction,<sup>†</sup> i.e. along the non symmetric cell parameter, by summing the contributions from the inorganic atoms lying on the same crystallographic plane. We excluded the organic atoms since they do not contribute to the frontier orbitals.<sup>23</sup> In this way, we obtained the local DOS associated to a specific  $i$ -th layer,  $DOS_i(t,E)$ , as in Ref. 33. In Figure 7, we report the  $DOS_i(t,E)$  for the paraelectric MA  $\beta$ 3 structure, in the energy range of the frontier levels, calculated for two consecutive geometries extracted from the AIMD simulations (time difference 0.06 ps) between 7 and 8 ps simulation time. The valence and conduction states are mainly localized for values of the  $c$ -axis of 0.00, 12.66, 18.99 and 25.32 Å, in correspondence of layers containing the largest number of inorganic atoms and show no localization in the initial optimized structure.<sup>33</sup> As shown in the Figure 7, in the first selected geometry occurring at ca. 7 ps, the valence band (VB) and conduction band (CB) edges are clearly localized in the layers lying respectively at 12.66 Å and at 0.00 Å. After just 0.06 ps instead, the localization of the electronic states is different, with the valence and conduction band edges localized respectively on the 6.33 Å and 18.99 Å lying layers. Thus, Figure 7 points out that the valence and conduction band edges may localize in spatially separated regions with a very fast, sub-ps, dynamics. This effect could play an important role on the photovoltaic working mechanism of MAPbI<sub>3</sub>, for instance, in relation to the exciton and/or charge separation mechanism.<sup>20,36</sup> Figure 7 suggests in fact that, subsequently to the photon absorption, the photo-generated species may diffuse in spatially separated regions of the material. Recent DFT calculations reported by Ma et. al.<sup>70</sup> pointed out a similar space-localization of the valence and conduction states of the MAPbI<sub>3</sub> perovskite, as a result of the random orientation of the MA cations. These authors also found that such a spatial-localization is much more evident in the case of large models (1728 MA cations). The computational cost of AIMD simulations limits the dimension of the present model to only 32 MA cations; however, it is interesting to note that the state localization is

noticeable also at this spatial scale. It is also worth to mention that Ma et. al. fixed the inorganic framework to the tetragonal structure.<sup>70</sup> For very large models, with a random orientation of the MA cations, the assumption of small relaxation of the inorganic framework seems reasonable but, on the other side, it could results in the overestimation of the spatial-localization of the electrons, because of the lack of indirect screening introduced by the relaxation of the inorganic cage.

Finally, our calculations highlight that the present localization is dynamical in nature, with a clear change of the valence and conduction edge position in only 0.06 ps (see Figure 7). This short time corresponds to frequencies of the order of hundreds of  $\text{cm}^{-1}$ , i.e much faster than the fastest motion of the inorganic component,<sup>14</sup> and thus the localization of the valence and conduction states in Figure 7 can be likely associated to the dynamics of the MA cations.

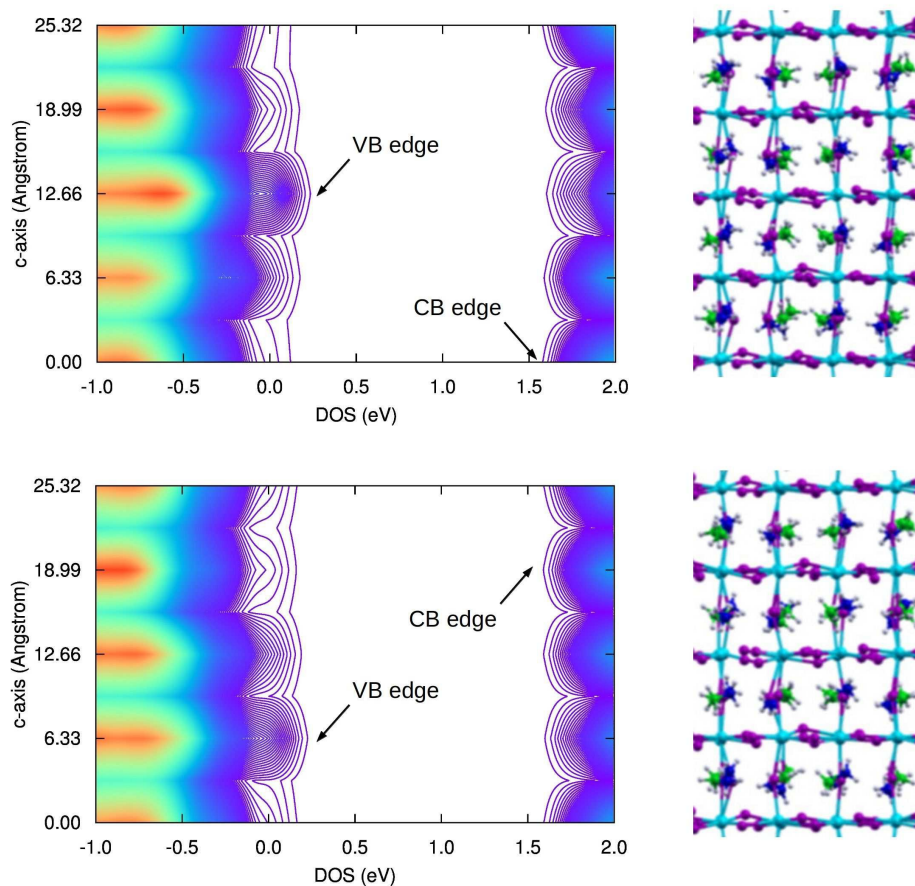


**Figure 7.** Surface plot of the density of states of the valence and conduction states for the various layers within the reference cell, for the MA  $\beta 3$  structure, for two consecutive geometries (0.06 ps time difference). The corresponding structure is reported on the right. The arrows indicate the spatial localization of the valence band (VB) and conduction (CB) edge.

Now, for each structure, we provide a general picture on the localization of the electronic states among the various layers, during the AIMD simulations. To quantify the electronic localization layer-by-layer, we calculate  $q_i(t,E)$ , that corresponds to the difference between the number of states at the LUMO energy,  $\text{DOS}_i(t,E=LUMO)$ , and the number of states at the HOMO energy,  $\text{DOS}_i(t,E=HOMO)$ , for the  $i$ -th layer; in mathematical form:

$$q_i(t) = \text{DOS}_i(t,E=LUMO) - \text{DOS}_i(t,E=HOMO)$$

Positive/negative values correspond to an excess of conduction/valence states in a given layer.

The evolution of the  $q_i(t,E)$  parameter for the investigated structures is reported in Figure 8 and it shows that the spatial localization of the valence and conduction band edges in a specific layer, as that reported in Figure 7, is quite common. Moreover, it confirms that the present mechanism is characterized by sub-ps dynamics ( $\sim 200 \text{ cm}^{-1}$ ), that is reasonably related to the libration motions of the MA cations. In Ref. 36, Even and coworkers suggested a role of collective MA cation motions on exciton screening, leading to almost free charges. Once again, the limited dimension of our models, mainly imposed by the computational cost of our approach, does not allow us to catch the effect of collective MA motions. Anyway, our AIMD simulations highlight a very local effect of the motion of the organic cations on the electronic properties, resulting in the separation of the electronic states within a few pseudo-cubic units.

In general, we observe a more effective localization for the conduction states than for valence states. It is interesting to note that MA  $\beta 1$ , characterized by the lower mobility of the MA cation, shows the smallest variations for  $q_i(t,E)$ , between 5 and -2. The MA  $\beta 3$  structure, characterized by more mobile MA cations, shows much larger oscillations for  $q_i(t,E)$ , between 12 and -4. The present result highlights once more the importance of the dynamic disorder on this dynamically driven state separation mechanism. It is worth to mention that MA  $\beta 1$  and MA  $\beta 2$  possess respectively a ferroelectric and antiferroelectric orientation of the MA cations and a polarization of  $4.41 \mu\text{C}/\text{cm}^2$  and nearly 0 has been calculated for these structures, respectively.<sup>33</sup> The presence of bulk polarization and the bulk polarization photovoltaic effect for structural models similar to the present MA  $\beta 1$  and MA  $\beta 2$  has been widely discussed by Zheng et. al. in Ref. 34. The case of MA  $\beta 2$  is probably the most interesting, since it shows a static localization of the valence and conduction bands at the layers lying respectively at  $0.00 \text{ \AA}$  and  $12.66 \text{ \AA}$ , which is directly related to the peculiar starting orientation of the MA cations, see Figure 8. In fact, the frontier states localize in correspondence of the interface of two

domains with opposite alignment of the MA cations along the  $c$ -axis, which are expected to behave as two ferroelectric domains with opposite polarizations. Thus, the present result points out the role of the interface between domains with orientated molecules on the photovoltaic working mechanism of hybrid perovskites, recalling the model of the “ferroelectric-highways” proposed by Walsh and coworkers<sup>32</sup> and the recently reported domain wall effect on charge separation proposed by Rappe and coworkers.<sup>71</sup> On the other hand, such models rely on the presence of domain interfaces which are stable on very long time-scales, to be able to affect the photovoltaic mechanism. In this regard, it is necessary to further investigate on the presence and stability and these domains, in light of the picoseconds rotational dynamics of the MA cations.<sup>50,51</sup>

The FA $\alpha$  phase, characterized by the largest orientational mobility of the organic cations (see Table 1), shows the smallest oscillation of the  $q_i(t,E)$  parameter, between 3.5 and -1.5, excluding sporadic cases with a very strong localization of the valence states. It is worth to note that the smallest degree of charge separation, i.e. smallest values of  $q_i(t,E)$ , are found for the model with the smaller and the larger mobility of the MA cations, MA  $\beta$ 1 and FA $\alpha$ . This results point out on different localization mechanisms for the tetragonal and the cubic phase of hybrid, lead iodide perovskites. The rationale behind this result could be the aforementioned weakening of the hydrogen bonds, going from the tetragonal to the cubic structure (see Figure 4) that results in a less effective, hydrogen-bond induced, localization of the electronic states.

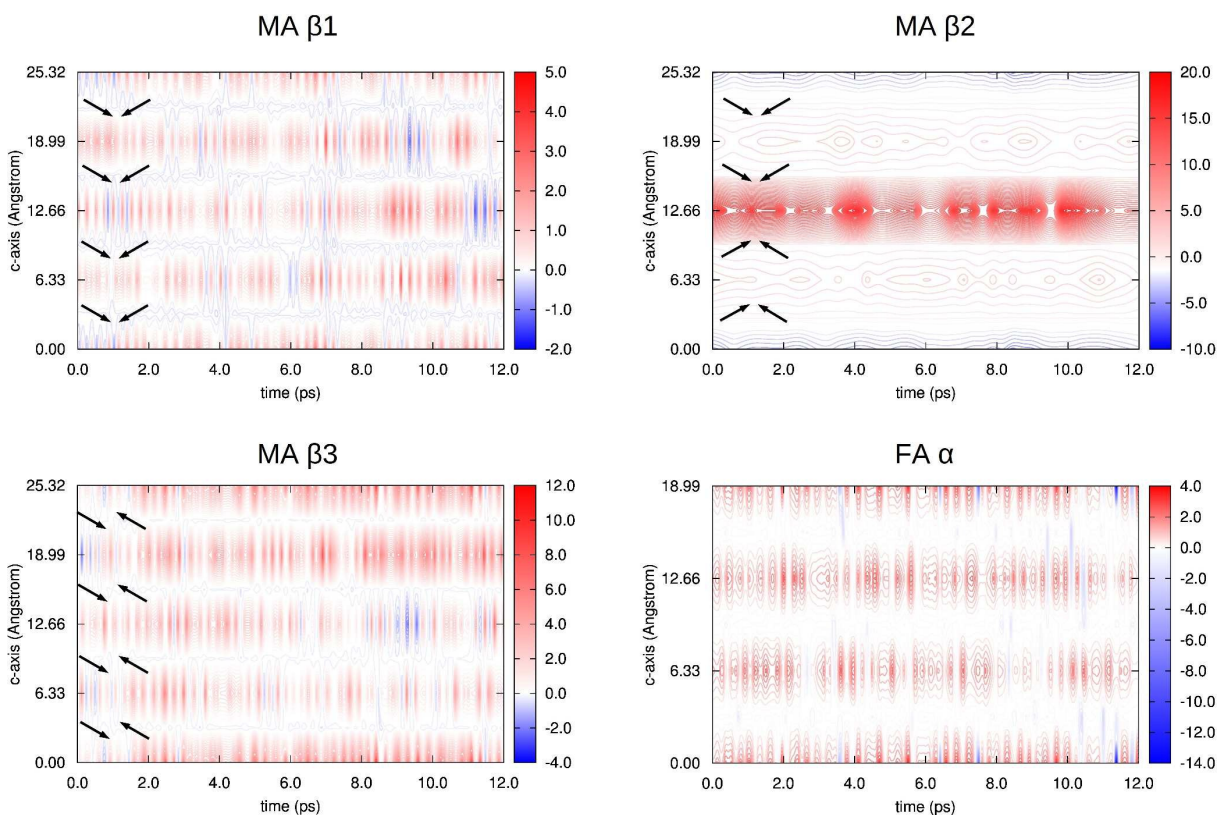


**Figure 8.** Evolution of the  $q_i(t)$  parameter (i.e. the difference between the number of states calculated at the LUMO and HOMO energy) for the MA  $\beta_1,2,3$ , and FA $\alpha$  structures. The arrows between 0-2ps represent the starting orientation of the MA cations, for the MA  $\beta_1,2,3$  structures.

#### 4. Conclusions.

In this perspective, we have illustrated the potential use of ab-initio molecular dynamics for the study of the structural and electronic properties of hybrid organic-lead halide perovskites, to elucidate the atomistic origin of the impressive photovoltaic properties of this class of materials. Ab-initio molecular dynamics are a powerful investigation tool, since they provide information on the electronic structure of the materials, taking the inherent structural dynamics into account. This feature is particularly relevant in the case of the hybrid organic-inorganic perovskites, where the presence of rotating organic cations within the cubo-cotahedral cavity,<sup>50,51</sup> and of the inherent “soft” nature of the inorganic framework are considerable.<sup>59,60</sup> As such, the local material structure can deviate significantly from the nominal structure of the material, from instance, the structure obtained from XRD measurements.<sup>30,57,58</sup>

Structural analyses of the molecular dynamics trajectories highlights the flexible structure of the hybrid lead iodide perovskite, MAPbI<sub>3</sub> and FAPbI<sub>3</sub>, demonstrating that the actual material structure can

deviate significantly with respect to the experimental structure from X-ray diffraction measurements. The latter in fact, represents a thermal averaged of different structures, characterized by a different organic cations orientations and octahedral rotation,<sup>62</sup> accessible within a time scale that is much longer with respect to the picosecond MA cation rotational dynamics. Together, our dynamics simulations outlined the different nature of the rotational motion of the MA/FA organic cations in the tetragonal and cubic phases, as due to a different balance between hydrogen bonds and thermally activate rotational motion. In the tetragonal phase, the presence of a strong hydrogen bond network keeps the organic cations oriented along specific directions, thus resulting in a re-orientational motion, from a strongly bound orientation to another. In the cubic phase instead, the thermal motion of the cation is stronger, resulting in a nearly free rotational motion of the cations within the cubo-octahedral cavity, in agreement with earlier results by Knop et. al.<sup>64</sup> Our results thus suggest a central role of the balance between specific organic-inorganic interactions (hydrogen bonds) and thermally activated motion in the transition from the tetragonal to the cubic crystalline structure. The estimated oscillation of the electronic levels and band gap, associated to the ion dynamics, has been set between 0.07 eV and 0.20 eV, to be compared with 0.40 eV of strongly disordered systems, as organic semiconductors and dye-sensitized interfaces.<sup>63</sup> Moreover, we found that the dynamic disorder from the ionic motion have important consequences on the electronic properties of hybrid, lead halide perovskites. The analysis of the localization of the electronic states demonstrates that a spatial separation of the valence and conduction states takes place in hybrid perovskites, during the molecular dynamics simulations. Such charge localization is obviously associated to a easier charge separation process, but can be also at the basis of the small charge recombination rates found in MAPbI<sub>3</sub>.<sup>19</sup> A similar evidence of electron state localization has been already pointed out by Ma et. al.,<sup>70</sup> using DFT calculations. In the present perspective however, we stress the dynamic character of such spatial localization of the valence and conduction states, which takes place on a sub-ps time scale. In other words, we address such spatial localization not to a static and disordered orientation of the organic cations but to their inherent rotational dynamics within the cubo-octahedral cavity. Thus, the mechanism of exciton screening due to the dynamics of the MA cation, hypothesized by Even in Ref. 36, finds here a demonstration from electronic structure calculations. Our calculations also show that in correspondence of borders between two domains with opposite alignment of the organic cations, there is a strong localization of valence/conduction states, thus demonstrating the “ferroelectric-highways” and the impact of domain walls on charge separation reported in the literature.<sup>33, 71</sup> We also highlight, however, the possible

instability of such configurations in light of the disorder generated in the material by the cation rotation at room temperature.

In summary, the huge amount of work devoted to understanding the structural and electronic features of hybrid lead-halide perovskites has delivered important information on the materials characteristics underlying their superior photovoltaic properties. In this context theoretical modeling and in particular ab initio molecular dynamics simulations may play a major role in further advancing the field of perovskite solar cells.

### Acknowledgments

The research leading to these results has received fundings from the European Union Seventh Framework Programme [FP7/2007%2013] under Grant Agreement No. 604032 of the MESO project.

### Notes and References

† For the  $FA\alpha$ , we chose the (111) planes, which are orthogonal to one of the pseudo-cubic axes.

1. J. Bisquert, The Swift Surge of Perovskite Photovoltaics, *J. Phys. Chem. Lett.* 2013, **4**, 2597–2598.
2. A. Kojima, K. Teshima, Y. Shirai, T. Miyasaka, Organometal Halide Perovskites as Visible-Light Sensitizers for Photovoltaic Cells, *J. Am. Chem. Soc.* 2009, **131**, 6050–6051.
3. A. M. Salau, Fundamental Absorption Edge in  $PbI_2:KI$  alloys, *Sol. Energy Mater.*, 1980, **2**, 327–332.
4. P. Gao, M. Grätzel and M. K. Nazeeruddin, Organohalide lead perovskites for photovoltaic applications, *Energy Environ. Sci.*, 2014, **7**, 2448.
5. J.-H. Im, C.-R. Lee, J.-W. Lee, S.-W. Park and N. G. Park, 6.5% efficient perovskite quantum-dot-sensitized solar cell, *Nanoscale* 2011, **3**, 4088–4093.
6. H.-S. Kim, C.-R. Lee, J.-H. Im, K.-B. Lee, T. Moehl, A. Marchioro, S.-J. Moon, R. Humphry-Baker, J.-H. Yum, J. E. Moser, Lead iodide perovskite sensitized all-solid-state submicron thin film mesoscopic solar cell with efficiency exceeding 9%. *Sci. Rep.* 2012, **2**, 591.
7. M. M. Lee, J. Teuscher, T. Miyasaka, T. N. Murakami and H. J. Snaith, Efficient hybrid solar cells based on meso-superstructured organometal halide perovskites. *Science* **2012**, **338**, 643–647.
8. J.-H. Heo, S.-H. Im, J.-H. Noh, T. N. Mandal, C.-S. Lim, J. A. Chang, Y.-H. Lee, H.-J. Kim, A. Sarkar, Md. K. Nazeeruddin, M. Grätzel and S.-I. Seok, Efficient inorganic–organic hybrid

- heterojunction solar cells containing perovskite compound and polymeric hole conductors. *Nature Photon.* 2013, **7**, 486–491.
9. J. Burschka, N. Pellet, S.-J. Moon, R. Humphry-Baker, P. Gao, Md. K. Nazeeruddin and M. Grätzel, Sequential deposition as a route to high-performance perovskite-sensitized solar cells. *Nature* 2013, **499**, 316–319.
10. M. Liu, M. B. Johnston and H. J. Snaith, Efficient planar heterojunction perovskite solar cells by vapour deposition. *Nature* 2013, **501**, 395–398.
11. H. Zhou, Q. Chen, G. Li, S. Luo, T.-B. Song, H.-S. Duan, Z. Hong, J. You, Y. Liu, Y. Yang, Interface engineering of highly efficient perovskite solar cells, *Science*, 2014, **345**, 542-546.
12. [www.nrel.gov/](http://www.nrel.gov/)
13. M. A. Green, A. Ho-Baillie and H. J. Snaith, The emergence of perovskite solar cells, *Nature Photon.* 2014, **8**, 506-514.
14. C. Quarti, G. Grancini, E. Mosconi, P. Bruno, J. M. Ball, M. M. Lee, H. J. Snaith, A. Petrozza, and F. De Angelis, The Raman Spectrum of the  $\text{CH}_3\text{NH}_3\text{PbI}_3$  Hybrid Perovskite: Interplay of Theory and Experiment, *J. Phys. Chem. Lett.* 2014, **5**, 279-284.
15. G. Grancini, S. Marras, M. Prato, C. Giannini, C. Quarti, F. De Angelis, M. De Bastiani, G. E. Eperon, H. J. Snaith, L. Manna, and A. Petrozza, The Impact of the Crystallization Processes on the Structural and Optical Properties of Hybrid Perovskite Films for Photovoltaics, *J. Phys. Chem. Lett.* 2014, **5**, 3836–3842.
16. E. Mosconi, C. Quarti, T. Ivanovska, G. Ruani and F. De Angelis, Structural and electronic properties of organo-halide lead perovskites: a combined IR-spectroscopy and ab initio molecular dynamics investigation, *Phys. Chem. Chem. Phys.* **2014**, **16**, 16137-16144.
17. S. D. Stranks, G. E. Eperon, G. Grancini, C. Menelaou, M. J. P. Alcocer, T. Leijtens, L. M. Herz, A. Petrozza, H. J. Snaith, Electron-Hole Diffusion Lengths Exceeding 1 Micrometer in an Organometal Trihalide Perovskite Absorber, *Science*, 2013, **342**, 341-344.
18. G. Xing, N. Mathews, S. Sun, S. S. Lim, Y. M. Lam, M. Grätzel, S. Mhaisalkar, T. C. Sum, Long-Range Balanced Electron-and Hole-Transport Lengths in Organic-Inorganic  $\text{CH}_3\text{NH}_3\text{PbI}_3$ , *Science*, 2013, **342**, 344-347.
19. C. Wehrenfennig, G. E. Eperon, M. B. Johnston, H. J. Snaith, and L. M. Herz, High Charge Carrier Mobilities and Lifetimes in Organolead Trihalide Perovskites, *Advanced Materials*, 2014, **26**, 1584-1589.

20. V. D'Innocenzo, G. Grancini, M. J. P. Alcocer, A. R. S. Kandada, S. D. Stranks, M. M. Lee, G. Lanzani, H. J. Snaith and A. Petrozza, Excitons versus free charges in organo-lead tri-halide perovskites, *Nature Commun.* 2014, **5**:3586
21. E. Edri, S. Kirmayer, A. Henning, S. Mukhopadhyay, K. Gartsman, Y. Rosenwaks, G. Hodes, D. Cahen, Why lead methylammonium tri-iodide perovskite-based solar cells require a mesoporous electron transporting scaffold (but not necessarily a hole conductor). *Nano Lett.* 2014, **14**, 1000–1004.
22. E. Edri, S. Kirmayer, S. Mukhopadhyay, K. Gartsman, G. Hodes and D. Cahen, Elucidating the charge carrier separation mechanism in  $\text{CH}_3\text{NH}_3\text{PbI}_{3-x}\text{Cl}_x$  perovskite solar cells. *Nature Commun.* 2014, **5**, 3461.
23. T. Umebayashi, K. Asai, T. Kondo and A. Nakao, Electronic structures of lead iodide based low-dimensional crystals, *Phys. Rev. B*, 2003, **67**, 155405.
24. E. Mosconi, A. Amat, Md. K. Nazeeruddin, M. Grätzel, and F. De Angelis, First-Principles Modeling of Mixed Halide Organometal Perovskites for Photovoltaic Applications, *J. Phys. Chem. C* 2013, **117**, 13902–13913.
25. J. Even, L. Pedesseau, J.-M. Jancu, and C. Katan, Importance of Spin–Orbit Coupling in Hybrid Organic/Inorganic Perovskites for Photovoltaic Applications, *J. Phys. Chem. Lett.* 2013, **4**, 2999–3005.
26. P. Umari, E. Mosconi and F. De Angelis, Relativistic GW calculations on  $\text{CH}_3\text{NH}_3\text{PbI}_3$  and  $\text{CH}_3\text{NH}_3\text{SnI}_3$  Perovskites for Solar Cell Applications, *Sci. Rep.* 2013, **4**, 4467.
27. a) F. Brivio, K. T. Butler, A. Walsh and M. van Schilfhaarde, Relativistic quasiparticle self-consistent electronic structure of hybrid halide perovskite photovoltaic absorbers, *Phys. Rev. B*, 2014, **89**, 155204; b) M. R. Filip, F. Giustino, *Phys. Rev. B*, 2014, **90**, 245145.
28. E. Menendez Proupin, P. Palacios, P. Wahnou, and J. C. Conesa, Self-consistent relativistic band structure of the  $\text{CH}_3\text{NH}_3\text{PbI}_3$  perovskite, *Phys. Rev. B*, 2014, **90**, 045207.
29. M. Kim, J. Im, A. J. Freeman, J. Ihm and H. Jin, Switchable  $S = 1/2$  and  $J = 1/2$  Rashba bands in ferroelectric halide perovskites, *Proceedings of the National Academy of Sciences*, 2014, **111**, 6900-6904.
30. C. C. Stoumpos, C. D. Malliakas and M. G. Kanatzidis, Semiconducting Tin and Lead Iodide Perovskites with Organic Cations: Phase Transitions, High Mobilities, and Near-Infrared Photoluminescent Properties, *Inorg. Chem.*, 2013, **52**, 9019–9038.
31. Y. Kutes, L. Ye, Y. Zhou, S. Pang, B. D. Huey and N. P. Padture, *J. Phys. Chem. Lett.*, 2014, **5**, 3335-3339.

32. J. M. Frost, K. T. Butler, F. Brivio, C. H. Hendon, M. van Schilfgaarde and A. Walsh, *Nano Letters* 2014, **14**, 2584–2590.
33. C. Quarti, E. Mosconi and F. De Angelis Interplay of Orientational Order and Electronic Structure in Methylammonium Lead Iodide: Implications for Solar Cell Operation, *Chem. Mater.* 2014, **26**, 6557–6569.
34. F. Zheng, H. Takenaka, F. Wang, N. Z. Koocher and A. M. Rappe, First-Principles Calculation of the Bulk Photovoltaic Effect in  $\text{CH}_3\text{NH}_3\text{PbI}_3$  and  $\text{CH}_3\text{NH}_3\text{PbI}_{3-x}\text{Cl}_x$ , *J. Phys. Chem. Lett.* 2015, **6**, 31–37.
35. A. Stroppa, D. Di Sante, P. Barone, M. Bokdam, G. Kresse, C. Franchini, M.-H. Whangbo and Silvia Picozzi, Tunable ferroelectric polarization and its interplay with spin–orbit coupling in tin iodide perovskites, *Nature Commun.*, 2014, **5**:5900.
36. J. Even, L. Pedesseau and C. Katan, Analysis of Multivalley and Multibandgap Absorption and Enhancement of Free Carriers Related to Exciton Screening in Hybrid Perovskites, *J. Phys. Chem. C* 2014, **118**, 11566–11572.
37. J. M. Frost, K. T. Butler and A. Walsh, Molecular ferroelectric contributions to anomalous hysteresis in hybrid perovskite solar cells. *APL Materials* 2014, **2**, 081506.
38. J. Ma and L.-W. Wang, Nanoscale Charge Localization Induced by Random Orientations of Organic Molecules in Hybrid Perovskite  $\text{CH}_3\text{NH}_3\text{PbI}_3$ , *Nano Lett.*, DOI: 10.1021/nl503494y.
39. G. Giorgi, J.-I. Fujisawa, H. Segawa and K. Yamashita, Cation Role in Structural and Electronic Properties of 3D Organic–Inorganic Halide Perovskites: A DFT Analysis, *J. Phys. Chem. C* 2014, **118**, 12176–12183.
40. V. Roiati, E. Mosconi, A. Listorti, S. Colella, G. Gigli and F. De Angelis, Stark Effect in Perovskite/ $\text{TiO}_2$  Solar Cells: Evidence of Local Interfacial Order, *Nano Lett.*, 2014, **14**, 2168–2174.
41. E. Mosconi, E. Ronca and F. De Angelis, First-Principles Investigation of the  $\text{TiO}_2$ /Organohalide Perovskites Interface: The Role of Interfacial Chlorine, *J. Phys. Chem. Lett.* 2014, **5**, 2619–2625.
42. S. Colella, E. Mosconi, P. Fedeli, A. Listorti, F. Gazza, F. Orlandi, P. Ferro, T. Besagni, A. Rizzo, G. Calestani, G. Gigli, F. De Angelis and R. Mosca,  $\text{MAPbI}_{3-x}\text{Cl}_x$  Mixed Halide Perovskite for Hybrid Solar Cells: The Role of Chloride as Dopant on the Transport and Structural Properties, *Chem. Mater.* 2013, **25**, 4613–4618.
43. G. Giorgi, J.-I. Fujisawa, H. Segawa and K. Yamashita, Small Photocarrier Effective Masses Featuring Ambipolar Transport in Methylammonium Lead Iodide Perovskite: A Density Functional

- Analysis, *J. Phys. Chem. Lett.* 2013, **4**, 4213–4216.
44. Jing Feng and Bing Xiao, Crystal Structures, Optical Properties, and Effective Mass Tensors of  $\text{CH}_3\text{NH}_3\text{PbX}_3$  ( $X = \text{I}$  and  $\text{Br}$ ) Phases Predicted from HSE06, *J. Phys. Chem. Lett.*, 2014, **5**, 1278-1282.
45. M. H. Du, Efficient carrier transport in halide perovskites: theoretical perspectives, *J. Mater. Chem. A*, 2014, **2**, 9091–9098.
46. J. Kim, S.-H. Lee, J. H. Lee and K.-H. Hong, The Role of Intrinsic Defects in Methylammonium Lead Iodide Perovskite, *J. Phys. Chem. Lett.*, 2014, **5**, 1312, 1317.
47. Y. Wang, T. Gould, J. F. Dobson, H. Zhang, H. Yang, X. Yao and H. Zhao, Density functional theory analysis of structural and electronic properties of orthorhombic perovskite  $\text{CH}_3\text{NH}_3\text{PbI}_3$ , *Phys. Chem. Chem. Phys.*, 2014, **16**, 1424-1429.
48. D. A. Egger and L. Kronik, Role of Dispersive Interactions in Determining Structural Properties of Organic–Inorganic Halide Perovskites: Insights from First-Principles Calculations, *J. Phys. Chem. Lett.* 2014, **5**, 2728–2733.
49. W. Geng, L. Zhang, Y.-N. Zhang, W.-M. Lau and L.-M. Liu, First-Principles Study of Lead Iodide Perovskite Tetragonal and Orthorhombic Phases for Photovoltaics, *J. Phys. Chem. C.*, 2014, **118**, 19565-19571.
50. A. Poglitsch and D. Weber, Dynamic Disorder in Methyl-ammoniumtrihalogenoplumbates(II) Observed by Millime-terwave Spectroscopy, *J. Chem. Phys.*, 1987, **87**, 6373–6378.
51. R. E. Wasylshen, O. Knop and J. B. Macdonald, Cation Rotation in Methylammonium Lead Halides, *Solid State Commun.*, 1985, **56**, 581–582.
52. R. Lindblad, D. Bi, B.-W. Park, J. Oscarsson, Mihaela Gorgoi, H. Siegbahn, M. Odellius, E. M. J. Johansson, and H. Rensmo, Electronic Structure of  $\text{TiO}_2/\text{CH}_3\text{NH}_3\text{PbI}_3$  Perovskite Solar Cell Interfaces, *J. Phys. Chem. Lett.* 2014, **5**, 648-653.
53. R. Car and M. Parrinello, Unified Approach for Molecular Dynamics and Density-Functional Theory". *Physical Review Letters*, 1985, **55**, 2471–2474.
54. P. Giannozzi, S. Baroni, N. Bonini, M. Calandra, R. Car, C. Cavazzoni, D. Ceresoli, G. L. Chiarotti, M. Cococcioni, I. Dabo, A. Dal Corso, S. de Gironcoli, S. Fabris, G. Fratesi, R. Gebauer, U. Gerstmann, C. Gougoussis, A. Kokalj, M. Lazzeri, L. Martin-Samos, N. Marzari, F. Mauri, R. Mazzarello, S. Paolini, A. Pasquarello, L. Paulatto, C. Sbraccia, S. Scandolo, G. Sclauzero, A. P. Seitsonen, A. Smogunov, P. Umari, and R. M. Wentzcovitch, QUANTUM ESPRESSO: a Modular and Open-Source Software Project for Quantum Simulations of Materials. *J. Phys: Condens. Matter* 2009, **21**, 395502.

55. J. P. Perdew, K. Burke and M. Ernzerhof, Generalized Gradient Approximation Made Simple. *Phys. Rev. B* 1996, **77**, 3865-3868.
56. D. Vanderbilt, Soft self-consistent pseudopotentials in a generalized eigenvalue formalism. *Phys. Rev. B*, 1990, *41*, 7892-7895.
57. Structural Study on Cubic-Tetragonal Transition of  $\text{CH}_3\text{NH}_3\text{PbI}_3$ , Y. Kawamura, H. Mashiyama and K. Hasebe, *J. Phys. Soc. Jpn.*, 2002, **71**, 1694–1697.
58. T. Baikie, Y. Fang, J. M. Kadro, M. Schreyer, F. Wei, Subodh G. Mhaisalkar, M. Graetzel and T. J. White, Synthesis and crystal chemistry of the hybrid perovskite  $(\text{CH}_3\text{NH}_3)\text{PbI}_3$  for solid-state sensitised solar cell applications, *J. Mater. Chem. A*, 2013, **1**, 5628–5641.
59. J. J. Choi, X. Yang, Z. M. Norman, S. J. L. Billinge, and J. S. Owen, Structure of Methylammonium Lead Iodide Within Mesoporous Titanium Dioxide: Active Material in High-Performance Perovskite Solar Cells, *Nano Lett.* 2014, **14**, 127–133.
60. R. Worhatch, H.-J. Kim, I. P. Swainson, A. L. Yonkeu and S. J. L. Billinge, Study of Local Structure in Selected Organic–Inorganic Perovskites in the  $\text{Pm}3\text{m}$  Phase, *Chem. Mater.* 2008, **20**, 1272–1277.
61. M. T. Weller, P. Henry, O. Weber, A. Di Pumpo and T. Hansen, Complete Structure and Cation Orientation in the Perovskite Photovoltaic Methylammonium Lead Iodide between 100 and 352 K, *Chem. Commun.* DOI: 10.1039/C4CC09944C.
62. A. M. Glazer, The Classification of Tilted Octahedra in Perovskites, *Acta Cryst.* 1972, **B28**, 3384-3392.
63. A. Amat, E. Mosconi, E. Ronca, C. Quarti, P. Umari, Md. K. Nazeeruddin, M. Grätzel and F. De Angelis, Cation-Induced Band-Gap Tuning in Organohalide Perovskites: Interplay of Spin–Orbit Coupling and Octahedra Tilting, *Nano Lett.* 2014, **14**, 3608–3616.
64. O. Knop, R. Wasylishen, E. M. White, T. S. Cameron and M. J. M. Van Oort, Alkylammonium lead halides. Part 2.  $\text{CH}_3\text{NH}_3\text{PbX}_3$  ( $\text{X} = \text{Cl}, \text{Br}, \text{I}$ ) perovskites: cuboctahedral halide cages with isotropic cation reorientation, *Can. J. Chem.* 1990, **68**, 412-422.
65. F. De Angelis, S. Fantacci and R. Gebauer, Simulating Dye-Sensitized  $\text{TiO}_2$  Heterointerfaces in Explicit Solvent: Absorption Spectra, Energy Levels, and Dye desorption, *J. Phys. Chem. Lett.*, 2011, **2**, 813–817.
66. G. C. Papavassiliou, I. B. Koutselas, Structural, Optical and Related Properties of Some Natural Three- And Lower-Dimensional Semiconductor Systems, *Synth. Met.* 1995, **71**, 1713–1714.
67. N. Kitazawa, Y. Watanabe, Y. Nakamura, Optical Properties of  $\text{CH}_3\text{NH}_3\text{PbX}_3$  ( $\text{X} = \text{halogen}$ ) and

- Their Mixed-Halide Crystals. *J. Mater. Sci.*, 2002, **37**, 3585–3587.
68. K. Tanaka, T. Takahashi, T. Bana, T. Kondo, K. Uchida, N. Miura, Comparative study on the excitons in lead-halide-based perovskite-type crystals  $\text{CH}_3\text{NH}_3\text{PbBr}_3$   $\text{CH}_3\text{NH}_3\text{PbI}_3$ , *Solid State Commun.* 2003, **127**, 619–623.
69. G. E. Eperon, S. D. Stranks, C. Menelaou, M. B. Johnston, L. M. Herz and H. J. Snaith, Formamidinium lead trihalide: a broadly tunable perovskite for efficient planar heterojunction solar cells, *Energy. Environ. Sci.* 2014, **7**, 982-988.
70. J. Ma, L. W.-Wang, Nanoscale charge localization induced by random orientations of organic molecules in hybrid perovskite  $\text{CH}_3\text{NH}_3\text{PbI}_3$ , *Nano Lett.* 2015, **15**, 248-253.
71. S. Liu, F. Zheng, N. Z. Koocher, H. Takenaka, F. Wang, and A. M. Rappe, Ferroelectric Domain Wall Induced Band Gap Reduction and Charge Separation in Organometal Halide Perovskites, *J. Phys.. Chem. Lett.* 2015, **6**, 693-699.

**Authors biographies and fotos.**

**Claudio Quarti** earned his Master Degree and his PhD in Materials Engineering at the Politecnico di Milano, in the group of vibrational spectroscopy Castiglioni-Zerbi. After, he spent one year and a half as a post-doc at the CNR-ISTM of Perugia, under the supervision of Dr. Filippo De Angelis. There, he was devoted to the study of structural and electronic of hybrid perovskite for photovoltaic applications. Recently, he gained a post-doc position at the University of Mons. His main research interests are the study of opto-electronic properties and the spectroscopic response of systems in the condensed phase, through first principle calculations.



**Edoardo Mosconi** obtained his Ph.D. degree in 2011 in theoretical chemistry from University of Perugia under the supervision of Prof. Antonio Sgamellotti and Dr. Filippo De Angelis, working on Computational Modeling of Hybrid/Organic Photovoltaics and Complex Reaction Mechanisms. From January 2012 he is a Post Doctoral Researcher at CNR Institute of Molecular Sciences and Technology (ISTM-CNR) in Perugia, at the Computational Laboratory for Hybrid/Organic Photovoltaics (CLHYO). His main research interests are in the field of new generation photovoltaics (Dye Sensitized Solar Cells, Organic Photovoltaics, and Perovskite Solar Cells), employing DFT, TDDFT, ab initio Car-Parrinello molecular dynamics and GW methods to predict and interpret the optical and electronic

properties of materials and interfaces.



**Filippo De Angelis** is senior research scientist and deputy director at the CNR Institute of Molecular Sciences and Technology, in Perugia, Italy. He is the founder and co-leader of the Computational Laboratory for Hybrid/Organic Photovoltaics in Perugia. He earned a B.S. in Chemistry 1996 and a PhD in Theoretical Inorganic Chemistry in 1999, both from the University of Perugia, Italy. He is an expert in the development and application of first principles computational methods to the simulation of the structural, electronic and optical properties of metallorganic, inorganic and hybrid materials and molecules and related interfaces. The main application studies are in the field of solar energy materials, with emphasis on dye-sensitized and perovskite solar cells. His main contribution constitutes in the study of the excited states of dyes and perovskite absorbers, in the modelling of inorganic semiconductors and in the alignment of energy levels at sensitized semiconductor interfaces. Additional areas of expertise are in the field of non-linear optics, luminescent materials for OLEDs and organometallic reactivity and catalysis. He is the 2007 recipient of the Raffaello Nasini Gold Medal of the Inorganic Chemistry Division of the Italian Chemical Society.